Research on Power Decoupling and Optimal Control of Modular Multiactive Bridge Converter With Relay Port

Changyu Gao, *Graduate Student Member, IEEE*, Kai Li, *Member, IEEE*, Zhibo Zhang, *Graduate Student Member, IEEE*, Fan Yuan, *Graduate Student Member, IEEE*, Sheng Zhang, Xiaojie You, *Member, IEEE*, and Chenchen Wang, *Senior Member, IEEE*

***Abstract*—Modular multiactive bridge (MMAB) converter is a modular, scalable, and promising multiport converter that facilitates flexible interconnection among various power sources and loads. In the conventional MMAB configuration, all ports are coupled to a common high-frequency link through multiple high-frequency transformers, which inherently induces cross-coupling power flow between ports. This article proposed a modified MMAB converter structure incorporating an additional relay port to achieve hardware-level power decoupling. The proposed topology does not require a complex control strategy and allows each port to operate independently as an individual dual-active bridge converter without interaction. The principle of power flow decoupling is analyzed in detail using frequency-domain analysis. Furthermore, an optimal design and control method based on duty ratio control is proposed to expand the zero-voltage switching operating range of the converter. The proposed structure also effectively suppresses the high-frequency oscillation within the MMAB converter. Finally, simulation and experimental results were obtained from different test scenarios to verify the power decoupling performance and the proposed control strategy.**

***Index Terms*—High-frequency oscillation (HFO), modular multiactive bridge converter (MMAB), multiport converter, power decoupling, zero-voltage switching (ZVS).**

I. Introduction

RECENTLY, multiport converters (MPCs) with high power density have gained widespread adoption across various applications, such as solid-state transformers in ac–dc hybrid distribution systems [1], [2], integrated energy system with electrolytic hydrogen production [3], electric vehicles [4], more-electrical aircraft [5], and traction power system [6], [7]. Compared to the conventional approach using multiple converters, an MPC provides a cost-effective, flexible, and efficient power processing solution by employing a single power conversion stage. The multiactive bridge (MAB) converter, a typical isolated MPC topology, utilizes a single multiwinding transformer to couple all ports [8]. However, the fixed design of the multiwinding transformer inherently limits port standardization and scalability. Subsequently, a promising topology named modular multiactive bridge (MMAB) converter was introduced in [9] and [10]. In this topology, the multiwinding high-frequency transformer (HFT) of the MAB converter is split into multiple two-winding HFTs. The MMAB converter consists of multiple H-bridge connected to the common high-frequency link (HFL) via multiple HFTs. The obvious advantage of this topology is easy modularity and high scalability. It is beneficial to design and manufacture, and the ports can be connected and disconnected from the system at any time [11].

The dynamic performance of the MPCs has constantly been a focal point in the literature. However, sharing magnetic components or high-frequency links among different ports reduces the total number of components, while inherently introducing power cross-coupling among different ports. This cross-coupling degrades dynamic performance and increases the control complexity. Consequently, the control structure of a multiport converter is a multi-input–multi-output (MIMO) system.

Various solutions for decoupling the power flow within the MAB converter and MMAB converter have been explored, broadly categorized into software-control-level methods and hardware-level methods [12]. Software-control-level decoupling methods have been extensively investigated for the MAB converters. According to the classical linear control theory, a preselected feed-forward compensator decoupling method was introduced in [7], [13], and [14]. This method mitigates loop interaction using a precalculated decoupling gain matrix, which is stored as a lookup table in the controller. However, constructing this decoupling matrix demands an accurate small-signal model and precise operating points for the converter, which poses a significant challenge. Another decoupling method was introduced in [1] and [15], which employs different control loop bandwidths for each port to achieve decoupling. In this approach, the high-bandwidth loop dictates the power flow direction during transients and minimizes interference from other ports, whereas

Received 29 May 2024; revised 20 August 2024 and 14 October 2024; accepted 22 November 2024. Date of publication 27 November 2024; date of current version 28 January 2025. This work was supported by the National Key Research and Development Program of China under Grant 2023YFB4004600. Recommended for publication by Associate Editor D. Oliveira. *(Corresponding author: Kai Li.)*

The authors are with the School of Electrical Engineering, Beijing Jiaotong University, Beijing 100044, China (e-mail: changyugao@bjtu.edu.cn; kaili@bjtu.edu.cn; zbzhang@bjtu.edu.cn; 20117035@bjtu.edu.cn; 23121514@bjtu.edu.cn; xjyou@bjtu.edu.cn; chchwang@bjtu.edu.cn).

Color versions of one or more figures in this article are available at https://doi.org/10.1109/TPEL.2024.3506745.

Digital Object Identifier 10.1109/TPEL.2024.3506745

the low-bandwidth loop has weaker anti-interference performance. A hybrid method combining a feed-forward compensator with varying bandwidth control loops was proposed in [5]. Furthermore, a time-sharing control strategy was proposed in [16], where only two ports operate simultaneously, while the others function as diode rectifiers. However, this method increases output voltage ripple and current stress, reducing overall power density. The small-signal model presented in [17] demonstrates the highly nonlinear characteristics of the MAB converter. Various nonlinear control techniques have been implemented to effectively decouple power flow and improve dynamic performance. Among these, model predictive control has gained significant attention for MAB converters [18], [19], [20]. Additionally, several other methods, such as linear active disturbance rejection control [21], sliding mode controller [22], supertwisting algorithm based on extended state observer [23], and online offline Newton decoupling algorithm [24], have also been proposed to achieve power flow decoupling.

The aforementioned software-control-level decoupling methods present a challenging tradeoff between complexity and dynamic performance. Consequently, several hardware-level decoupling methods with good decoupling performance and simple control strategy have been introduced. The fundamental concept of hardware-level decoupling is modifying the equivalent impedance of each port. Bandyopadhyay et al. [25] proposed a decoupling scheme that decreases the series phase-shift inductance at a specific input-power port, which must remain connected to a stiff-voltage source. However, this method restricts power flow direction due to the predetermined allocation of phase-shift inductance between the input and output ports during the design stage. Other hardware decoupling methods involve inserting various series resonant circuits into the converter and selecting a resonant frequency equal to the switching frequency [26], [27], [28]. Because these topologies are predetermined, power flow direction remains limited. To address this limitation, techniques like the "switch-controlled capacitor" [29] and the "variable inductor" [30] are employed in series resonant circuits to adjust the resonant frequency based on the operating mode. Although these schemes decouple power flows, they pose significant challenges in terms of control implementation and system reliability.

This article proposes a modified structure for the MMAB converter that effectively mitigates the inherent cross-coupling power by introducing an additional port. In this topology, the decoupling port is directly connected to the HFL without HFT or phase-shift inductor, acting as an intermediary station that temporarily receives power from source ports and forwards it to load ports. This is analogous to a "relay node" in networking, which functions as an intermediary for transmitting data between network segments. Henceforth, this additional decoupling port is referred to as the "relay port". The characteristics and contributions of the proposed decoupling structure are as follows.

1) The proposed topology achieves hardware-level power decoupling with a simple control strategy, providing exceptional dynamic performance.
2) The proposed topology exhibits high scalability and sufficient fault tolerance, with bidirectional and independently controllable ports. Moreover, these ports can be connected or disconnected from the system at any time without affecting the normal operation of other ports.
3) The proposed converter achieves zero-voltage switching (ZVS) across the full operating range through optimal design and control method.
4) The proposed structure effectively eliminates the high-frequency oscillation (HFO) in the MMAB converter.

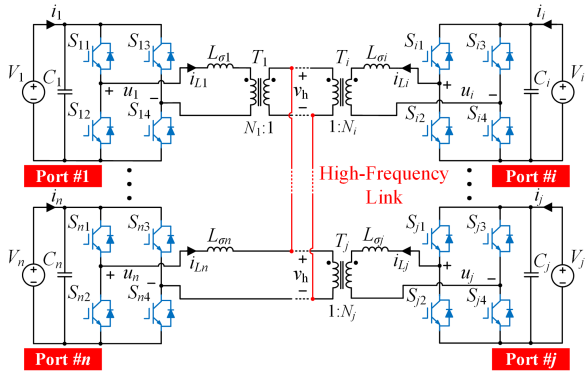

Fig. 1. Schematic of the n-port MMAB converter.

The rest of this article is organized as follows. Section II introduces the operational theory and power flow analysis of the MMAB converter. Section III presents a decoupling structure of the MMAB converter, along with the principle of power flow decoupling. Section IV details an optimal design and control method for achieving ZVS in the converter. The topology's characteristic of suppressing HFO is discussed in Section V. Sections VI and VII provide simulation and experimental results to validate the proposed scheme. Finally, Section VIII concludes this article.

II. Theory of MMAB Converter

A. MMAB Topology and Waveforms

The n-port MMAB converter is composed of n H-bridge cells and (n-1) independent HFTs. These HFTs are connected in parallel to a common high-frequency link. The schematic is shown in Fig. 1. For port #i ($i = 1, 2, \ldots, n$), N_i represents the ratio of transformer T_i. $L_{\sigma i}$ is the sum of leakage inductance of HFT and the phase-shift inductance. S_{i1}–S_{i4} are the switches. C_i is the dc-side capacitance of the H-bridge. u_i is the ac terminal voltage. i_{Li} is the inductor current. V_i is the dc terminal voltage. i_i is the dc terminal current. $v_{\rm h}$ is the HFL voltage.

For convenience, the n-port MMAB converter circuit shown in Fig. 1 can be simplified into the Y-type equivalent circuit depicted in Fig. 2(a) by replacing the output voltage of each port with an ac square voltage source and integrating it with the transformer's T-type equivalent model. For port #i, the output ac voltage u_i, inductor current i_{Li}, and equivalent leakage inductance $L_{\sigma i}$ and magnetizing inductance $L_{{\rm m}i}$ are referred to the HFL side, e.g.,

$$u_i' = u_i/N_i, \quad i_{Li}' = N_i i_{Li}, \quad L_{\sigma i}' = N_i^2 L_{\sigma i}. \tag{1}$$

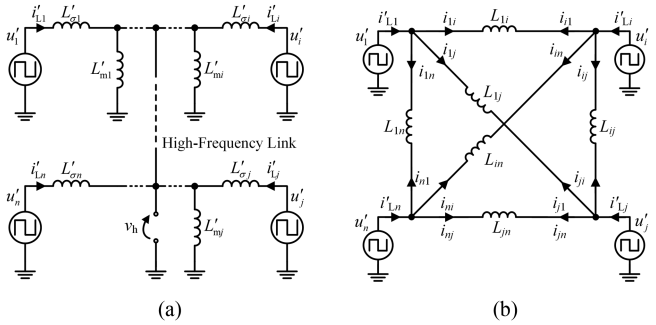

Fig. 2. n-port MMAB converter equivalent circuits. (a) Y-type circuit. (b) Δ-type circuit.

The ac voltage of the HFL is derived from the superposition of output voltages from all ports, resulting in a complex variable. Therefore, the Y-type circuit is not suitable for analyzing the power flow between ports. A Δ-type equivalent circuit is utilized based on Thevenin's theorem, as shown in Fig. 2(b). The transmission power for each port is determined by the superposition of power from the relevant branches. The total power for the port #i in the MMAB converter is calculated as

$$P_i = \sum_{i \neq j}^{n} P_{ij} \tag{2}$$

where P_{ij} is the power from port #i to port #j.

According to the Thevenin's theorem, the equivalent link inductance L_{ij} between port #i and port #j can be expressed as

$$L_{ij} = L'_i L'_j \left(\sum_{l=1}^{n} \frac{1}{L'_l} + \sum_{l=1}^{n-1} \frac{1}{L_{\mathrm{ml}}} \right). \tag{3}$$

To enhance system control flexibility and optimize performance, the MMAB converter employs multiple phase-shift (MPS) modulation. Each port features two control degrees of freedom: 1) the outer phase-shift angle φ and 2) the inner phase-shift ratio d. The inner phase-shift ratio d_i refers to the phase shift between the switches S_{i1} and S_{i4} of port #i. The outer phase-shift angle φ_i represents the phase shift between port H-bridge output ac voltage u_1 and u_i (i.e., the phase shift between their fundamental components). The typical output voltage waveforms from the H-bridge of each port are illustrated in Fig. 3.

B. Power Flow Analysis

The power flows between ports in an MMAB converter are complex due to the multiple ports and multiple control degrees of freedom, especially under MPS modulation. When employing time-domain analysis, it is necessary to classify and discuss the various operating modes of the MMAB converter, which significantly increases the analytical complexity. However, since periodic variations are observed in the steady-state characteristics of each port, a frequency-domain analysis is a more suitable approach for evaluating the converter's behavior.

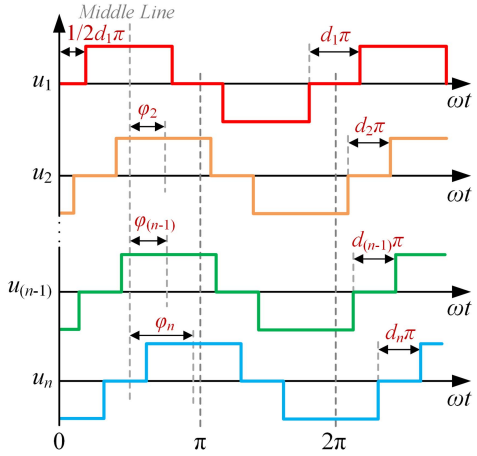

Fig. 3. Typical output voltage waveforms of the conventional n-port MMAB converter under MPS modulation.

In frequency-domain analysis, the periodic ac voltages and currents can be analytically represented using Fourier series. According to Fourier series superposition, the H-bridge output voltage of port #i can be expressed as

$$u_i(t) = \sum_{k=1,3,5,\ldots} \frac{4V_i}{k\pi} \cos\left(\frac{kd_i\pi}{2}\right) \sin\left(k\left(\omega_s t - \varphi_i\right)\right) \tag{4}$$

where $\omega_s = 2\pi f_s$, and f_s is the switching frequency. The output port voltage of each port can be decomposed into a combination of odd-order harmonic components, utilizing simple sine, and cosine functions.

From Fig. 2(b), two port voltages u_i and u_j are connected across an inductor. The instantaneous current i_{ij} between port #i and #j in Δ-type circuit can be calculated as

$$\begin{aligned} i_{ij}(t) &= \int \frac{u'_i(t) - u'_j(t)}{L_{ij}} dt \\ &= \sum_{k=1,3,5,\ldots} \frac{4}{k^2\pi\omega_s L_{ij}} \left[\begin{pmatrix} \frac{V_j}{N_j} \cos\left(\frac{kd_j\pi}{2}\right)\cos\left(k\varphi_j\right) \\ -\frac{V_i}{N_i} \cos\left(\frac{kd_i\pi}{2}\right)\cos\left(k\varphi_i\right) \end{pmatrix} \cos\left(k\omega_s t\right) \right. \\ &\quad \left. + \begin{pmatrix} \frac{V_j}{N_j} \cos\left(\frac{kd_j\pi}{2}\right) \sin\left(k\varphi_j\right) \\ -\frac{V_i}{N_i} \cos\left(\frac{kd_i\pi}{2}\right) \sin\left(k\varphi_i\right) \end{pmatrix} \sin\left(k\omega_s t\right) \right]. \end{aligned} \tag{5}$$

Applying Kirchhoff's current law at port #i, the inductor current for port #i can be expressed as

$$\begin{aligned} i_{\mathrm{L}i}(t) &= \frac{1}{N_i} i'_{Li}(t) = \frac{1}{N_i} \sum_{j=1, j\neq i}^{n} i_{ij}(t) \\ &= \sum_{j=1, j\neq i}^{n} \sum_{k=1,3,5,\ldots} \frac{4}{k^2 N_i \pi \omega_s L_{ij}} \\ &\quad \left[\begin{pmatrix} \frac{V_j}{N_j} \cos\left(\frac{kd_j\pi}{2}\right) \cos\left(k\varphi_j\right) \\ -\frac{V_i}{N_i} \cos\left(\frac{kd_i\pi}{2}\right) \cos\left(k\varphi_i\right) \end{pmatrix} \cos\left(k\omega_s t\right) \right. \\ &\quad \left. + \begin{pmatrix} \frac{V_j}{N_j} \cos\left(\frac{kd_j\pi}{2}\right) \sin\left(k\varphi_j\right) \\ -\frac{V_i}{N_i} \cos\left(\frac{kd_i\pi}{2}\right) \sin\left(k\varphi_i\right) \end{pmatrix} \sin\left(k\omega_s t\right) \right]. \end{aligned} \tag{6}$$

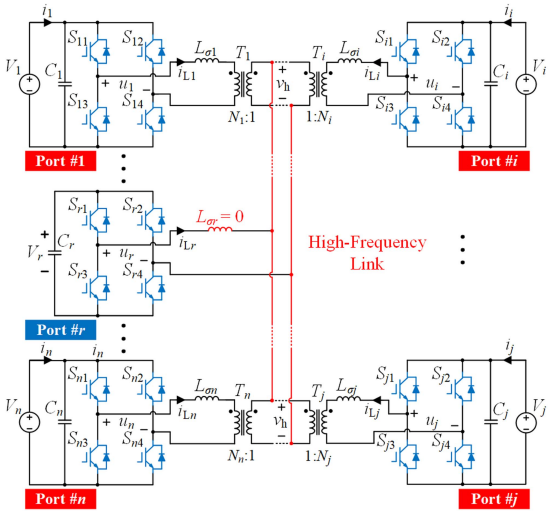

Fig. 4. Schematic of the proposed MMAB converter with decoupling structure.

By combining (4) and (6), the active power for port #*i* over one switching cycle can be described as

$$P_i = \frac{1}{T_s}\int_0^{T_s} v_i(t) i_{Li}(t) dt = \sum_{j=1,\, j\neq i}^{n} \sum_{k=1,3,5,\ldots} \frac{8 V_i V_j}{k^3 \pi^2 N_i^2 \omega_s L_{ij}} \cos\left(\frac{k d_i \pi}{2}\right) \cos\left(\frac{k d_j \pi}{2}\right) \times \sin\left[k\left(\varphi_j - \varphi_i\right)\right]. \tag{7}$$

According to (7), the power flow of the port #*i* is influenced not only by its own dc port voltage, outer phase-shift angle, and inner phase-shift ratio, but also by those of other ports and the equivalent link inductance. This interdependency causes inherent cross-coupling of power flows between ports, affecting both the dynamic and steady-state performance of the converter.

III. Decoupling Structure and Control Strategy

A. Proposed Structure

In this section, a modified structure of the MMAB converter is proposed to address the issue of inherent cross-coupling power flow between ports by introducing an additional relay port.

As discussed in Section II, the interport power of the MMAB converter is influenced by the equivalent link inductance between each port. For an *n*-port MMAB converter, only (*n*-1) individual two-winding HFTs are required to provide isolation among the ports, while the remaining port is connected to the HFL via a high-frequency phase-shift inductor. Fig. 4 illustrates the proposed MMAB converter with decoupling structure. Compared to the conventional MMAB converter, the port without an individual HFT (i.e., port #*r*) eliminates the high-frequency phase-shift inductor and directly connects to the HFL.

The port #*r*, hereinafter referred to as relay port, operates with zero active power consumption and does not deliver power through the dc terminal. The relay port maintains the stable dc terminal voltage through phase shift control from a source port, which is supplied by the constant voltage source. Furthermore, the relay port functions as an intermediary station, temporarily holding, and forwarding power. It receives power from the source ports and transfers it to the load ports, maintaining the power balance within the converter, i.e.,

$$\sum P_{\text{Source Port}} + \sum P_{\text{Load Port}} = 0. \tag{8}$$

By setting the port inductance $L_{\sigma r}$ to zero and directly connecting the H-bridge in parallel to the HFL, the output square-wave voltage of the relay port effectively clamps the voltage of the HFL, ensuring that $u_r = v_h$. Consequently, the HFL of the MMAB converter operates as a high-frequency ac microgrid. The relay port is typically positioned internally within the converter and remains inaccessible externally, which minimizes the likelihood of failure due to external factors. In contrast, nonrelay ports are externally connected to the HFL. In the event of a failure in an external nonrelay port, the port can be deactivated and removed from the system without affecting the normal operation of the relay port or other nonrelay ports. This design significantly enhances the reliability of the converter system.

B. Principle of Power Decoupling

The principle of power decoupling method using a relay port is introduced in this section. According to (7), the equivalent link inductance has a significant influence on the power flow of port #*i*. The proposed MMAB converter structure represents a special case where the conventional topology is modified by removing the high-frequency inductor from one port. As depicted in Fig. 4, the inductor of the relay port #*r* is removed, resulting in $L_{\sigma r} = 0$. This modification simplifies the expression for the equivalent link inductance L_{ij} as follows:

$$L_{ij} = \begin{cases} \text{NA}, & i = j \\ L'_{\sigma j}, & i = r, j \neq r \\ L'_{\sigma i}, & i \neq r, j = r \\ \infty, & i \neq r, j \neq r, i \neq j. \end{cases} \tag{9}$$

The inductor current of port #*i* can be rewritten as

$$i_{Li} = \begin{cases} \frac{1}{N_i}\sum_{j=1, j\neq r}^{n} i_{rj} \\ = \sum_{j=1, j\neq r}^{n} \sum_{k=1,3,5,\ldots} \frac{4}{k^2 \pi \omega_s L'_{\sigma j}} \\ \quad \times \left[\begin{pmatrix} \frac{V_j}{N_j} \cos\left(\frac{k d_j \pi}{2}\right) \cos\left(k\varphi_j\right) \\ -V_r \cos\left(\frac{k d_r \pi}{2}\right) \cos\left(k\varphi_r\right) \end{pmatrix} \cos\left(k\omega_s t\right) \right. \\ \quad \left. + \begin{pmatrix} \frac{V_j}{N_j} \cos\left(\frac{k d_j \pi}{2}\right) \sin\left(k\varphi_j\right) \\ -V_r \cos\left(\frac{k d_r \pi}{2}\right) \sin\left(k\varphi_r\right) \end{pmatrix} \sin\left(k\omega_s t\right) \right], i = r \\ \frac{1}{N_i} i_{ir} \\ = \sum_{k=1,3,5,\ldots} \frac{4}{k^2 \pi N_i \omega_s L'_{\sigma i}} \\ \quad \times \left[\begin{pmatrix} V_r \cos\left(\frac{k d_r \pi}{2}\right) \cos\left(k\varphi_r\right) \\ -\frac{V_i}{N_i} \cos\left(\frac{k d_i \pi}{2}\right) \cos\left(k\varphi_i\right) \end{pmatrix} \cos\left(k\omega_s t\right) \right. \\ \quad \left. + \begin{pmatrix} V_r \cos\left(\frac{k d_r \pi}{2}\right) \sin\left(k\varphi_r\right) \\ -\frac{V_i}{N_i} \cos\left(\frac{k d_i \pi}{2}\right) \sin\left(k\varphi_i\right) \end{pmatrix} \sin\left(k\omega_s t\right) \right], i \neq r. \end{cases} \tag{10}$$

The cycle-by-cycle average power P_{ij} from port #*i* to port #*j* in this MMAB converter configuration can be determined using (4), (5), and (9), as represented in

$$P_{ij}=\begin{cases}\sum_{k=1,3,5,\dots}\frac{8V_rV_j}{k^3\pi^2\omega_sL'_{\sigma j}}\cos\left(\frac{kd_r\pi}{2}\right)\cos\left(\frac{kd_j\pi}{2}\right)\\ \times\sin\left[k\left(\varphi_j-\varphi_r\right)\right], & i=r,j\neq r\\ \sum_{k=1,3,5,\dots}\frac{8V_iV_r}{k^3\pi^2N_i^2\omega_sL'_{\sigma i}}\cos\left(\frac{kd_i\pi}{2}\right)\cos\left(\frac{kd_r\pi}{2}\right)\\ \times\sin\left[k\left(\varphi_r-\varphi_i\right)\right], & i\neq r,j=r\\ 0, & i\neq r,j\neq r,i\neq j.\end{cases}\tag{11}$$

According to (11), the power flows within the MMAB converter with the decoupling structure are categorized into two cases: 1) power flow between the relay port #*r* and nonrelay ports, and 2) power flow between two nonrelay ports. However, there is no power flow between the nonrelay ports. The nonrelay ports employ phase-shift control to regulate their individual power flows by referencing the output voltage phase of the relay port, where both the outer phase-shift angle φ_r and the inner phase-shift ratio d_r of the relay port are fixed at zero. The active power of port #*i* can be rewritten as

$$P_i=\begin{cases}\sum_{j=1,j\neq r}^{n}\sum_{k=1,3,5,\dots}\frac{8V_rV_j}{k^3\pi^2\omega_sL'_{\sigma j}}\cos\left(\frac{kd_j\pi}{2}\right)\sin(k\varphi_j), & i=r\\ -\sum_{k=1,3,5,\dots}\frac{8V_iV_r}{k^3\pi^2N_i^2\omega_sL'_{\sigma i}}\cos\left(\frac{kd_i\pi}{2}\right)\sin\left(k\varphi_i\right), & i\neq r.\end{cases}\tag{12}$$

As previously discussed, the power of the relay port #*r* is equivalent to the sum of the power flows in the relevant branches. Conversely, the power of nonrelay port is determined solely by its own circuit parameters, without being affected by the other nonrelay ports. Consequently, this configuration enables independent control of the nonrelay ports, effectively eliminating the cross-coupling power between the nonrelay ports.

C. Control Strategy for Proposed Suture

Fig. 5 illustrates the general control diagram of the proposed MMAB converter with a decoupling structure. This converter consists of two types of ports: 1) the relay port and 2) the nonrelay ports. The nonrelay ports are further categorized into source ports and load ports, depending on whether they inject power into or receive power from the converter.

The relay port, denoted as port #*r*, features its dc terminal is connected to a capacitor without any load, and its ac side directly interfaces in parallel with the HFL. The phase of its output ac square wave voltage serves as a reference for other ports by setting both the outer phase-shift angle φ_r and the inner phase-shift ratio d_r to zero. Assuming negligible switching and conduction losses, the relay port does not consume power and efficiently transfers power from source ports to load ports.

The source ports, such as port #1 and port #*i*, typically connect to stiff voltage sources, such as a dc microgrid or energy storage systems. These ports inject power into the MMAB converter

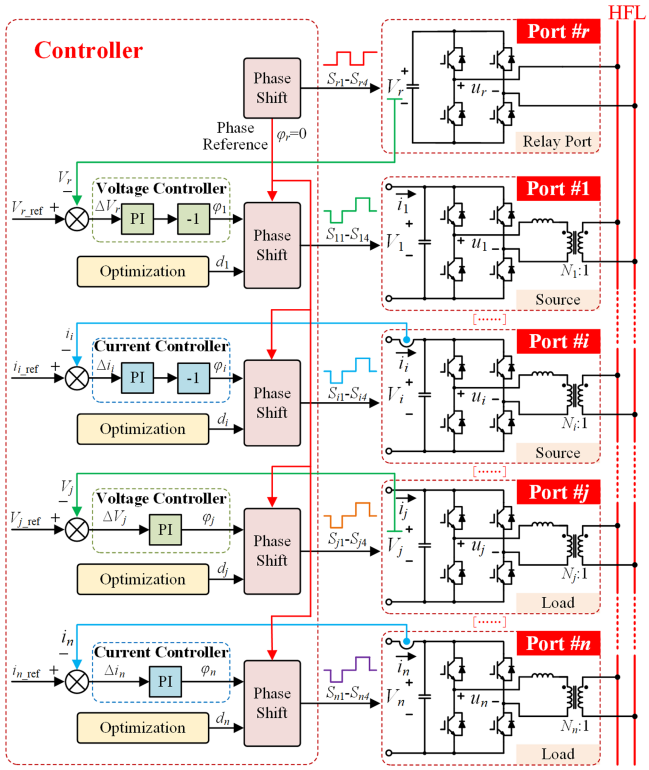

Fig. 5. General control diagram of the proposed MMAB converter with decoupling structure.

while stabilizing the relay port's dc terminal voltage. However, in converters with multiple source ports, only one port (e.g., port #1) employs a voltage controller to stabilize the relay port's dc terminal voltage, commonly referred to as a slack port. The difference between the voltage of the relay port's dc terminal V_r and the reference voltage V_{r_ref} is fed into a PI controller to regulate the outer phase-shift angle φ_1 of port #1. Other source ports (e.g., port #*i*) utilize current controllers to adjust the phase-shift angles φ_i based on current references i_{i_ref} and control the power injected into the MMAB converter.

The load ports, such as port #*j* and port #*n*, are classified into two types: 1) voltage-load ports (e.g., port #*j*), which connect to loads that require a stable dc voltage, and 2) current-load ports (e.g., port #*n*), which require a stable current. These ports receive power from the MMAB converter. Depending on the connected load type, either voltage or current closed-loop control is utilized to track output voltage or current reference by dynamically adjusting the phase-shift angle.

The output voltage waveforms of the MMAB converter with decoupling structure are shown in Fig. 6. The source ports waveforms lead that of the relay port, while the load port waveforms lag behind that of the relay port.

All non-relay ports possess bidirectional power transfer capabilities. A nonrelay port connected to a dc source can alternate between functioning as a source port or a load port by adjusting the phase-shift angle. This flexibility allows for dynamic management of power flow within the converter.

The power fluctuations at the load port affect the relay port's dc terminal voltage. According to (12), voltage perturbation in

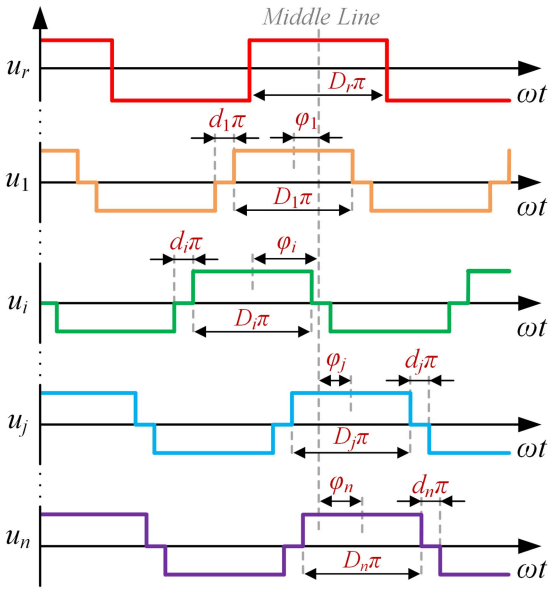

Fig. 6. Output voltage waveforms of the MMAB converter with decoupling structure.

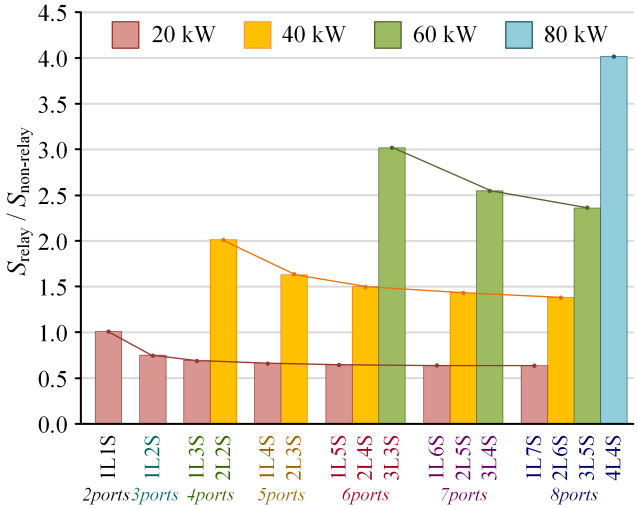

Fig. 7. Comparison of power ratings of relay port and nonrelay ports under different operating conditions.

the relay port subsequently influences the power flow across other ports. To mitigate this influence, the relay port's voltage control loop bandwidth is designed to be higher than that of other control loops. This configuration enables rapid adjustments of input power to the relay port and facilitates the efficient transfer of power fluctuations to the slack port, thereby minimizing inter-port interaction induced by load variations.

The proposed structure in this article decomposes a tightly-coupled MIMO multiport converter into multiple single-input–single-output (SISO) two-port converters. This approach enables the application of optimization strategies traditionally used for DAB converters, such as minimizing the root-mean-square (rms) value of inductor current, expanding the ZVS range, minimizing circulating power. Section IV introduces an optimal method for the proposed structure to expand the ZVS operating range.

D. Discussion on Port Power Rating

The relay port is connected directly to the high-frequency link without a high-frequency transformer or a phase-shift inductor, which limits the current rise. Additionally, the high-frequency current at the relay port is a cumulative sum of the high-frequency currents from all other nonrelay ports, leading to a higher high-frequency current in the relay port compared to other nonrelay ports. This section addresses the power rating of both the relay port and the nonrelay ports to provide insights for converter design.

As previously discussed, the relay port operates with zero active power consumption. Instead, the power associated with the relay port is entirely reactive, and its power rating is defined in terms of apparent power. The apparent power is expressed as follows:

$$S_i = u_{i(\text{rms})} \cdot i_{\text{L}i(\text{rms})} \tag{13}$$

where $u_{i(\text{rms})}$ is the rms value of the ac output voltage, and $i_{\text{L}i(\text{rms})}$ is the rms value of the ac output current. Here, $u_{i(\text{rms})}$ is approximately equal to the port dc voltage V_i, since the ac output voltage u_i is nearly a square wave. Based on (10), the rms value of the port ac current is given by

$$i_{\text{L}i(\text{rms})} = \sqrt{\frac{1}{T_s}\int_0^{Ts} i_{\text{L}i}(t)^2 dt}. \tag{14}$$

In practical engineering applications, the power modules of the nonrelay ports in the MMAB converter are typically equivalent, which facilitates modular design and manufacturing. It is assumed that each nonrelay port has an identical maximum power rating and the dc terminal voltages of both the relay and nonrelay ports are identical. Fig. 7 illustrates the ratios of the apparent power of the relay port to that of the non-relay ports for various MMAB converter configurations, considering different numbers of source (S) and load (L) ports. The number of all load ports is less than or equal to the number of source ports, with load ports operating at their maximum active power (20 kW) and all source ports are balanced to supply active power. Rectangles of the same color in the bar graph indicate configurations with equal total transmitted active power (20 kW, 40 kW, 60 kW, and 80 kW). The results indicate that the power rating of the relay port increases proportionally with the total transmitted active power of the converter. For a constant total transmitted active power (as indicated by the trend line of the same color in Fig. 7), the power rating of the relay port decreases as the number of nonrelay ports increases. Significantly, the power rating of the relay port reaches its maximum when the number of source ports and load ports is balanced.

IV. ZVS Optimal Method

The MMAB converters exhibit inherent ZVS conduction operation under phase-shift modulation, which significantly minimizes switching losses and enhances efficiency. Nonetheless, ZVS operation may be compromised under light load conditions,

especially when voltage conversion ratios among all ports are extremely unbalanced [31], [32]. Analysis in Section II highlights the complex operating characteristics of conventional MMAB converters under MPS modulation due to their multiple ports and the inherent coupling among them. This complexity presents challenges for optimal design and control. In this section, an optimal design and control method based on duty ratio control is proposed to expand the ZVS operating range. The ZVS operating conditions of the proposed MMAB converter with relay port are also analyzed.

A. Proposed ZVS Optimal Design and Control Method

In [33], the dc conversion ratio for the DAB converter is defined as

$$M = \frac{N_{\mathrm{p}} \cdot V_{\mathrm{s}}}{N_{\mathrm{s}} \cdot V_{\mathrm{p}}} \tag{15}$$

where N_{p} and N_{s} denote the turns of the primary and secondary winding of the transformer, respectively, and V_{p} and V_{s} represent the dc voltage of the primary and secondary winding, respectively. The DAB converter achieves ZVS over full operating range when the dc voltage conversion ratios on both sides match (i.e., $M = 1$). Additionally, a larger phase-shift angle facilitates the soft switching condition.

To expand the ZVS operating range, a duty ratio control method was proposed in [15]. The duty ratio D, as illustrated in Fig. 6, represents the pulse width of the output rectangular voltage waveform, where $D = 1 - d$. Moreover, the volt-second product refers to the multiplication of the pulse amplitude and duty ratio (i.e., $V{\cdot}D$). To achieve the maximum ZVS operating range for the DAB converter, it is essential to adjust the duty ratio to ensure volt-second balance between the primary and secondary sides, i.e.,

$$N_{\mathrm{s}} \cdot D_{\mathrm{p}} \cdot V_{\mathrm{p}} = N_{\mathrm{p}} \cdot D_{\mathrm{s}} \cdot V_{\mathrm{s}} \tag{16}$$

where D_{p} and D_{s} represent the duty ratios of the converter's primary and secondary voltages, respectively, with values ranging from 0 to 1.

Section III proposes a modified structure for the MMAB converter incorporating an additional relay port, which decomposes the n-port MMAB converter into n two-port DAB converters associated with the relay port. It effectively mitigates power cross-coupling among the nonrelay ports. As a result, the method of expanding the ZVS region used for the DAB converter can be applicable to the proposed MMAB structure. Specifically, duty ratio control can be independently implemented for each nonrelay port.

In the proposed structure, the relay port operates in a square-wave mode ($D_r = 1$) and is connected in parallel with the common HFL ($N_r = 1$). Consequently, the dc conversion ratio M_i of the nonrelay port #i can be expressed as

$$M_i = \frac{V_i}{N_i \cdot V_r}. \tag{17}$$

To satisfy the volt-second balance among the ports, the duty ratio control must ensure

$$N_i \cdot V_r = D_i \cdot V_i. \tag{18}$$

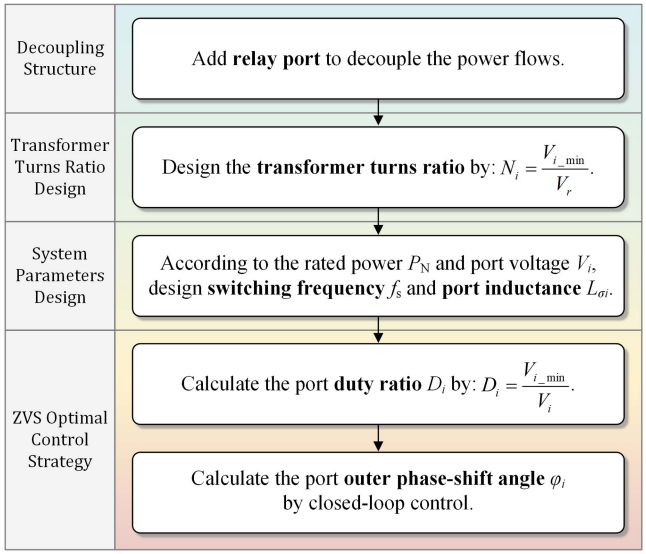

Fig. 8. Flowchart for the ZVS optimal design and control method.

The MMAB converter exhibits complex operating conditions due to significant voltage level differences and fluctuations across each port, especially when interfacing with supercapacitors or fuel cells. Thus, the ZVS operation range is significantly reduced.

It is assumed that the voltage V_i at port #i fluctuates between the minimum voltage $V_{i\_\min}$ and the maximum voltage $V_{i\_\max}$. To maintain the volt-second balance when the dc terminal voltage of nonrelay port is at its minimum, the transformer turns ratio N_i is designed according to

$$N_i = \frac{V_{i\_\min}}{V_r}. \tag{19}$$

Then the duty ratio is adjusted according to the real-time port voltage, expressed as

$$D_i = \frac{V_{i\_\min}}{V_i} = \frac{N_i V_r}{V_i}. \tag{20}$$

This ensures port #i always satisfies (18), where the volt-second products of the two voltages applied to the corresponding transformer windings remain balanced.

A flowchart for the ZVS optimal design and control method is presented in Fig. 8 achieve ZVS operation in the MMAB converter. The process begins with introducing a relay port to decouple the power flows within the MMAB converter. Subsequently, the transformer turns ratio is designed based on the minimum dc voltage of the nonrelay ports and the dc voltage of the relay port, as indicated in (19). Following this, key converter parameters, including the switching frequency f_{s} and port inductance $L_{\sigma i}$, are determined according to (12). During operation, the outer phase-shift angle is dynamically adjusted through closed-loop feedback to regulate power flow, while the duty ratio is precisely adjusted according to (20) to ensure ZVS. It is important to note that the duty ratio control loop operates at a slower rate than the power flow control loop.

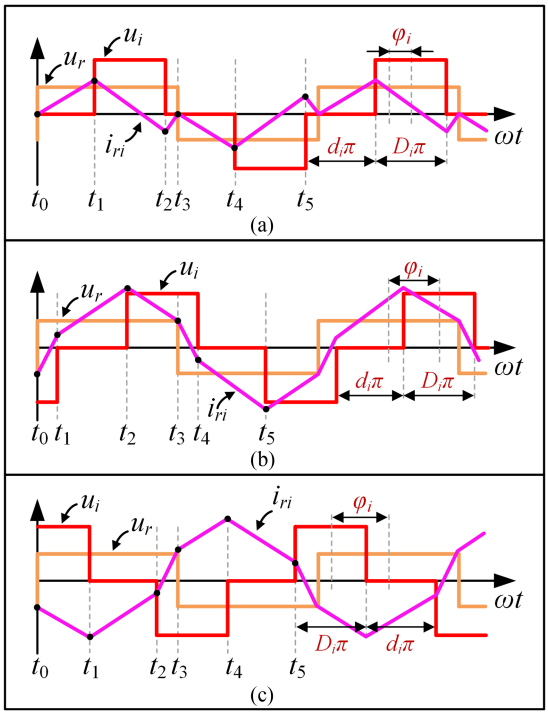

Fig. 9. Output voltage and current waveforms for the operation modes. (a) Inner mode. (b) Right-outer mode. (c) Left-outer mode.

B. Analysis of ZVS Conditions

In an MMAB converter with duty ratio control, the nonrelay port operates in two distinct modes: 1) inner mode and 2) outer mode. The boundary between these modes is defined by $\varphi_{i\_B} = \pi/2{\cdot}(1-D_i)$. Under light loads ($|\varphi_i| < \varphi_{i\_B}$), the port operates in the inner mode, while under heavy loads ($|\varphi_i| > \varphi_{i\_B}$), it operates in the outer mode. Fig. 9 illustrates the output voltage u_i and equivalent current i_{ri} waveforms for both operation modes. The equivalent currents i_{ri} between the port #r and port #i at the switching instants with duty ratio control are calculated as follows.

In inner mode

$$\begin{cases} i_{ri}(t_0) = 0, & i_{ri}(t_3) = 0 \\ i_{ri}(t_1) > 0, & i_{ri}(t_2) < 0,\ i_{ri}(t_4) < 0,\ i_{ri}(t_5) > 0 \end{cases}. \tag{21}$$

In right-outer mode

$$\begin{cases} i_{ri}(t_0) < 0, & i_{ri}(t_3) > 0 \\ i_{ri}(t_1) > 0, & i_{ri}(t_2) > 0,\ i_{ri}(t_4) < 0,\ i_{ri}(t_5) < 0 \end{cases}. \tag{22}$$

In left-outer mode

$$\begin{cases} i_{ri}(t_0) < 0, & i_{ri}(t_3) > 0 \\ i_{ri}(t_1) < 0, & i_{ri}(t_2) < 0,\ i_{ri}(t_4) > 0,\ i_{ri}(t_5) > 0 \end{cases}. \tag{23}$$

These calculated equivalent currents i_{ri} at the switching instants correspond to the current shown in Fig. 9.

The ZVS condition for each port is determined by the port inductor currents $i_{\mathrm{L}i}$ at the switching instants. Under ideal conditions, where deadtime and parasitic capacitance of the switches are neglected, ZVS for port #i is achieved when $i_{Li} < 0$ during the turn-ON of S_{i1} and S_{i4}, indicating that current flows through the parasitic body diodes of the switches. Table I summarizes the ZVS conditions for different ports based on the inductor current $i_{\mathrm{L}i}$. Due to the symmetry of inductor currents, any switch in the MMAB converter can achieve ZVS during every switching period.

TABLE I
ZVS CONDITIONS OF PORTS IN DIFFERENT OPERATIONS

Operation mode	ZVS Conditions	
	Relay Port	Non-relay Port
Inner mode	$i_{\mathrm{L}r}(t_0)<0$, $i_{\mathrm{L}r}(t_3)>0$	$i_{\mathrm{L}i}(t_1)<0$, $i_{\mathrm{L}i}(t_2)>0$, $i_{\mathrm{L}i}(t_4)>0$, $i_{\mathrm{L}i}(t_5)<0$
Right-outer mode		$i_{\mathrm{L}i}(t_1)<0$, $i_{\mathrm{L}i}(t_2)<0$, $i_{\mathrm{L}i}(t_4)>0$, $i_{\mathrm{L}i}(t_5)>0$
Left-outer mode		$i_{\mathrm{L}i}(t_1)>0$, $i_{\mathrm{L}i}(t_2)>0$, $i_{\mathrm{L}i}(t_4)<0$, $i_{\mathrm{L}i}(t_5)<0$

However, the relationship between the equivalent current i_{ri} and the inductor current $i_{\mathrm{L}i}$ is different for the nonrelay port and the relay port. For nonrelay port #i, the port inductor current $i_{\mathrm{L}i}$ is equal to the reverse equivalent current i_{ri} as defined by the reference direction in Fig. 2(b) ($i_{\mathrm{L}i} = -i_{ri}/N_i$). The instantaneous port inductor current $i_{\mathrm{L}i}$ in different operation modes can be expressed as (24), shown at the bottom of the next page.

Therefore, the ZVS conditions for nonrelay port #i are satisfied in both inner and outer modes, ensuring that ZVS is achieved across the full operating range.

For relay port #r, the inductor current $i_{\mathrm{L}r}$ is the sum of equivalent currents i_{ri} through each relevant branch, as follows:

$$i_{\mathrm{L}r} = \sum_{i=1, i\neq r}^{n} i_{ri}. \tag{25}$$

The ZVS conditions for relay port #r are determined by the equivalent currents i_{ri} from all relevant branches. According to (21), (22), and (23), only in the outer mode does the equivalent current i_{ri} contribute to the ZVS condition of the relay port. However, in the inner mode, the equivalent current i_{ri} becomes zero when the switches turn ON, resulting in the relay port operating in critically zero-current switching (ZCS). In this case, the equivalent current neither contributes to the ZVS condition nor worsens the switching condition.

From (25), as long as one of the nonrelay port dc voltages matches the relay port voltage ($M_i = 1$) or operates in the outer mode, the equivalent current i_{ri} will contribute to the relay port #r achieving ZVS. In conclusion, if the equivalent current i_{ri} through any branch meets the ZVS conditions, the inductor current in the relay port will certainly ensure ZVS operation.

Fig. 10 shows the ZVS boundaries for port #i and port #r across the entire operating range of the converter to effectively identify the ZVS operating regions. As depicted in Fig. 10(a), when the voltages are matched ($M_i = 1$), both the relay port #r and non-relay port #i can achieve ZVS over the full operating

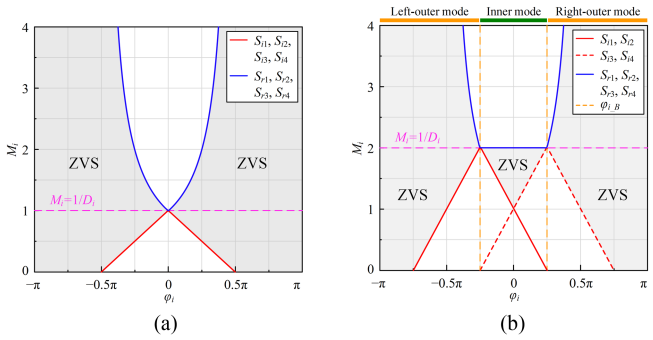

Fig. 10. ZVS boundaries for different values of D_i. (a) $D_i = 1$. (b) $D_i = 0.5$.

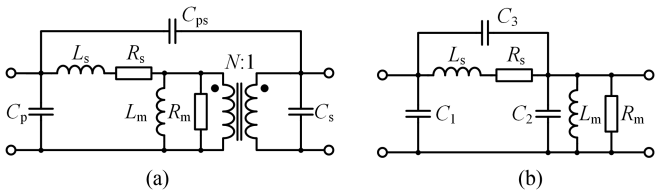

Fig. 11. Equivalent circuit of a HFT considering the stray parameters. (a) Equivalent circuit. (b) Equivalent circuit referred to the primary side.

range without duty ratio control. In Fig. 10(b), when the converter adopts the duty ratio control ($D_i = 1 / M_i$), the nonrelay port #*i* achieves ZVS over the full operating range. However, the relay port #*r* can achieve ZVS only in the outer mode, while it operates in critical ZCS in the inner mode.

V. High-Frequency Oscillation Suppression Method

In the DAB converter and MMAB converter, the parasitic capacitors of the HFT, combined with the leakage inductors and the phase-shift inductors, constitute undesirable high-frequency resonant tanks. These resonant tanks are susceptible to excitation by the high-frequency square-wave voltage generated by the H-bridge, leading to an undesirable high-frequency oscillation problem within the high-frequency link [34], [35]. This HFO problem can result in electro-magnetic interference and common mode noise, increasing the voltage stress on the transformer and causing waveform distortion. Accordingly, the proposed structure offers an effective method to suppress HFO within the HFL.

The H-bridge cell with HFT serves as the core unit in the MMAB converter. A classical π-shaped network with three capacitors is utilized to analyze the impedance of the oscillation tank, as depicted in Fig. 11(a). In this model, L_m denotes the magnetizing inductance, R_m represents the core loss equivalent resistance, L_s indicates the leakage inductance, R_s is the winding resistance, N is the turn ratio of HFT, C_p and C_s represent the self-capacitance of the primary and secondary windings, respectively, and C_ps denotes the mutual capacitance between the two windings. Furthermore, the parasitic capacitances of the HFT can be referenced to the primary side, as shown in Fig. 11(b). The capacitances in Fig. 11(b) can be correlated with the capacitances in Fig. 11(a) by [36]

$$\begin{cases} C_1 = C_\mathrm{p} - (1-N)\, C_\mathrm{ps}/N \\ C_2 = C_\mathrm{s}/N^2 - (1-N)\, C_\mathrm{ps}/N^2 \\ C_3 = C_\mathrm{ps}/N. \end{cases} \tag{26}$$

Thus, the equivalent impedance network for the MMAB converter with relay port is shown in Fig. 12. For port #*i*, $L_{\mathrm{ph}\,i}$ is the phase-shift inductance, and $R_{\mathrm{ph}\,i}$ is the equivalent resistance of the inductor. As shown in Fig. 12, the HFL voltage v_h results from the superposition of each port's ac voltage u_i, forming a complex multiple-input single-output (MISO) impedance network.

In the converter, the magnetizing inductance L_m of the HFT is large, and the phase-shift inductance L_ph is also much larger than the leakage inductance L_s, i.e., $L_\mathrm{m} >> L_\mathrm{s}$, $L_\mathrm{ph} >> L_\mathrm{s}$. Therefore, the influence of the magnetizing inductance and leakage inductance can be neglected, and a simplified model is obtained, as shown in Fig. 13. The simplified parasitic capacitances of the HFT can be expressed as follows:

$$C_i = C_{\mathrm{p}i} + C_{\mathrm{s}i}. \tag{27}$$

When analyzing the oscillation voltage excited by one source u_i, while other sources are short-circuited, Fig. 14 illustrates the SISO impedance network, where the equivalent distributed capacitance C_e, the equivalent magnetizing resistance R_me, and the equivalent impedance Z_s can be, respectively, expressed as

$$C_\mathrm{e} = \sum_{k=1}^{n} C_k \tag{28}$$

$$R_\mathrm{me} = 1/\sum_{k=1}^{n} \frac{1}{R_{\mathrm{m}k}} \tag{29}$$

$$Z_\mathrm{s} = 1/\sum_{k\neq i}^{n} \frac{1}{R_{\mathrm{ph}k} + sL_{\mathrm{ph}k}}. \tag{30}$$

In the equivalent impedance network shown in Fig. 14, $v_{\mathrm{h}\,i}$ represents the oscillating voltage within HFL under the excitation of the output ac voltage u_i of the port #*i*. The transfer function relating $v_{\mathrm{h}\,i}$ to u_i can be derived as: (31), shown at the bottom of the next page.

Using the superposition principle, the HFL voltage v_h can be obtained as: (32), shown at the bottom of the next page.

$$\begin{cases} i_{\mathrm{L}i}(t_1) < 0,\ i_{\mathrm{L}i}(t_2) > 0,\ i_{\mathrm{L}i}(t_4) > 0,\ i_{\mathrm{L}i}(t_5) < 0, & \text{Inner Mode} \\ i_{\mathrm{L}i}(t_1) < 0,\ i_{\mathrm{L}i}(t_2) < 0,\ i_{\mathrm{L}i}(t_4) > 0,\ i_{\mathrm{L}i}(t_5) > 0, & \text{Right-outer Mode} \\ i_{\mathrm{L}i}(t_1) > 0,\ i_{\mathrm{L}i}(t_2) > 0,\ i_{\mathrm{L}i}(t_4) < 0,\ i_{\mathrm{L}i}(t_5) < 0, & \text{Left-outer Mode.} \end{cases} \tag{24}$$

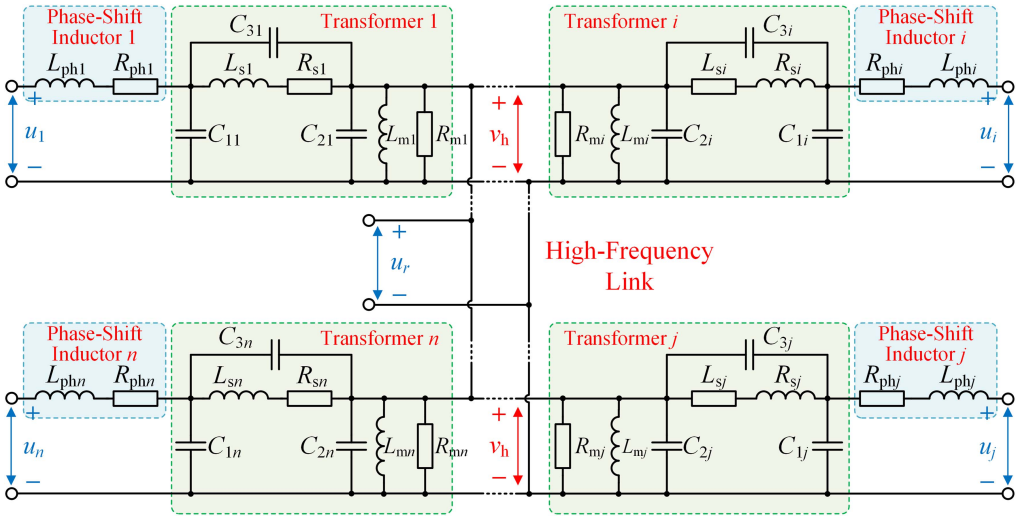

Fig. 12. Equivalent MISO impedance network of MMAB converter with a relay port.

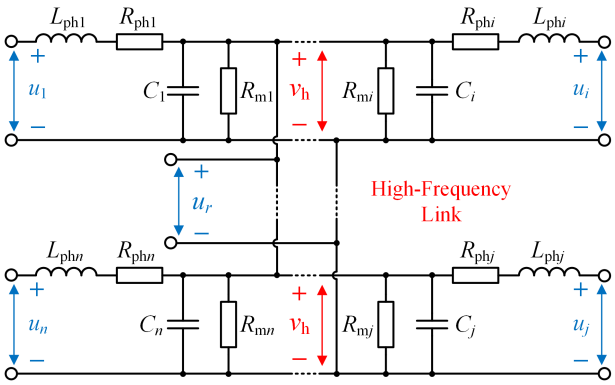

Fig. 13. Simplified model of MMAB converter.

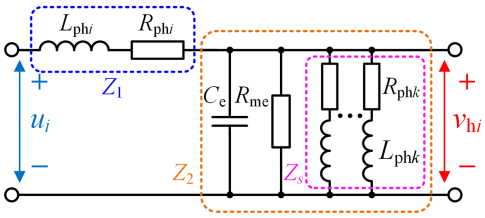

Fig. 14. Equivalent SISO impedance network with one input excitation.

From (32), the complexity of the HFO problem within the HFL escalates with an increasing number of ports in the MMAB converter.

However, in the proposed structure of MMAB, the relay port without a phase-shift inductor and HFT can be effectively utilized as the active clamping circuit connected to the HFL for voltage oscillation suppression. As a result, the HFL voltage is equal to the output ac voltage of relay port ($u_r = v_{\rm h}$).

VI. Simulation Verification

The proposed decoupling structure of the MMAB converter with a relay port and the ZVS optimal control method has been verified through simulation in PLECS. Furthermore, a circuit model was constructed in LTspice to evaluate the proposed HFO suppression method. The MMAB converter schematic used for the simulation is presented in Fig. 15. The system parameters for the simulation are detailed in Table II. The converter is comprised of four ports: two bidirectional voltage source ports, a load port, and a relay port. Port #1 acts as the slack port to maintain the stability of the dc terminal voltage at relay port #*r*. Port #2 employs a current controller to regulate the power injected into the converter. Port #3 employs a voltage control loop to maintain the voltage across a resistive load.

$$
\begin{aligned}
G_{{\rm h}i}(s) &= \frac{v_{{\rm h}i}(s)}{u_i(s)} = \frac{Z_2}{Z_1+Z_2} \\
&= \frac{1}{(R_{{\rm ph}i}+sL_{{\rm ph}i})\cdot\left(\sum_{k\neq i}^{n}\frac{1}{R_{{\rm ph}k}+sL_{{\rm ph}k}}+\sum_{k=1}^{n}\frac{1}{R_{{\rm m}k}}+\sum_{k=1}^{n}sC_k\right)+1}. \qquad (31)\\
v_{\rm h}(s) &= \sum_{i=1}^{n} v_{{\rm h}i}(s) = \sum_{i=1}^{n} G_{{\rm h}i}(s)\,u_i(s) \\
&= \sum_{i=1}^{n}\frac{v_i(s)}{(R_{{\rm ph}i}+sL_{{\rm ph}i})\cdot\left(\sum_{k\neq i}^{n}\frac{1}{R_{{\rm ph}k}+sL_{{\rm ph}k}}+\sum_{k=1}^{n}\frac{1}{R_{{\rm m}k}}+\sum_{k=1}^{n}sC_k\right)+1}. \qquad (32)
\end{aligned}
$$

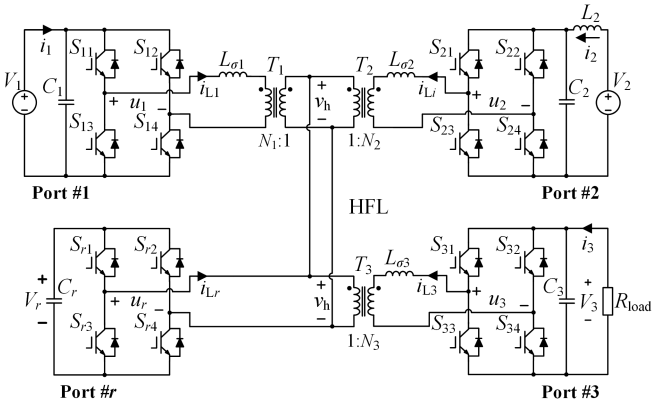

Fig. 15. Schematic of the MMAB converter with relay port for simulation.

TABLE II
SYSTEM ELECTRICAL PARAMETERS

Parameter	Value
Port dc terminal voltages V_1, V_2, V_3	150 V, 150 V, 150 V
Relay port dc terminal voltage V_r	150 V
Transformer ratios N_1, N_2, N_3	1:1, 1:1, 1:1
Switching frequency f_s	10 kHz
Equivalent inductances $L_{\sigma1}$, $L_{\sigma2}$, $L_{\sigma3}$	126 μH, 148 μH, 141 μH
H-bridge capacitances C_1, C_2, C_3, C_r	2.1 mF, 2.1 mF, 2.1 mF, 2.1 mF
LC filter inductance L_2	20 μH

A. Dynamic Behavior and Power Decoupling Validation

The simulations aim to demonstrate the efficacy of the proposed MMAB converter structure in terms of decoupling the power flows, enabling precise and independent control over the individual ports. Two case studies are discussed as follows.

1) *Case Study I*: A load step in the voltage-controlled port #3 is introduced to study the effect of the voltage loop on the efficacy of the current control loop.
2) *Case Study II*: A reference current step in the current-controlled port #2 is applied to investigate the effect of the current loop on the voltage loop.

Additionally, these simulations also involve a conventional three-port MMAB converter without the decoupling structure. The dynamic performance of the proposed MMAB converter is compared to that of the conventional MMAB converter to demonstrate the advantages of the proposed topology.

Case Study I: The simulations are carried out at the following operating point: $P_2 = -150$ W ($i_2 = -1$ A), $P_3 = -281$ W ($R_{\text{load}} = 80\ \Omega$). The dynamic response is tested by applying a load step at port #3. The load is increased by 50% ($R_{\text{load}} = 80\ \Omega$ to $40\ \Omega$, $P_3 = -281$ W to -562 W) at $t = 0.6$ s and then reverted to the initial value ($R_{\text{load}} = 40\ \Omega$ to $80\ \Omega$, $P_3 = -562$ W to -281 W) at $t = 1.0$ s. Fig. 16(a) illustrates the dynamic performance waveforms for different MMAB topologies during a load step. The results reveal that in the conventional MMAB converter, the current overshoot of port #2 is 1.36 A under an increasing load, and the current undershoot is 1.45 A when the load decreases. In contrast, the MMAB with the relay port shows minimal current variation. The simulation results demonstrate that the proposed decoupling structure achieves almost perfect decoupling despite the load fluctuating.

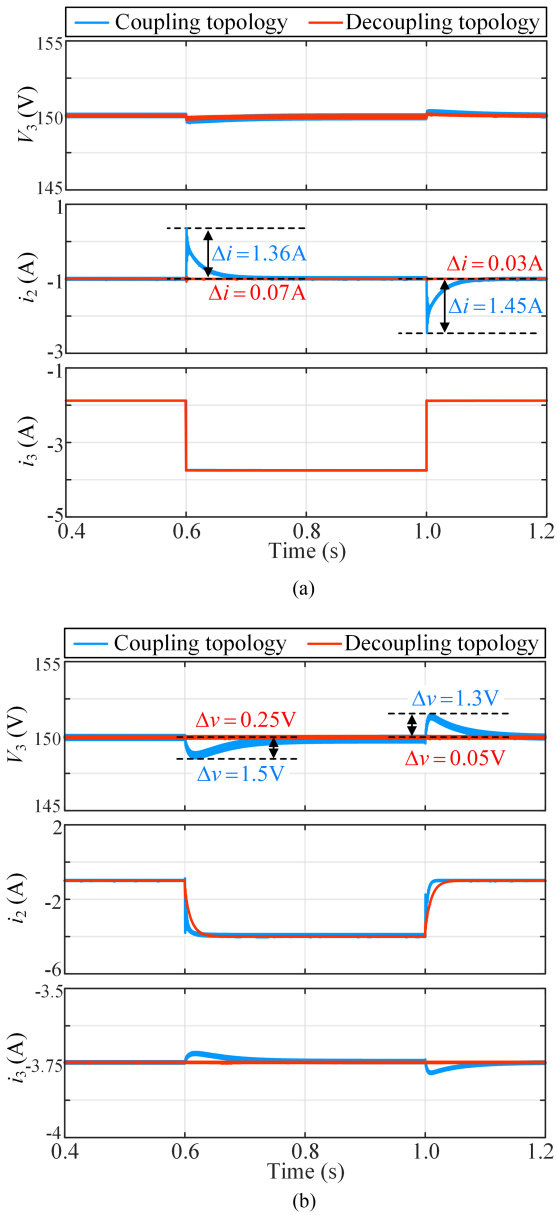

Fig. 16. Transient performance of port voltage and current in different topologies: conventional MMAB converter and proposed MMAB converter with relay port. (a) Case study I: A load step at port #3. (b) Case study II: A reference current changes at port #2.

Case Study II: The simulations are carried out at the following operating point: $P_2 = -150$ W ($i_2 = -1$ A), $P_3 = -562$ W ($R_{\text{load}} = 40\ \Omega$). The reference current at port #2 is changed from -1 A to -4 A ($P_2 = -150$ W to -600 W) at $t = 0.6$ s and then reverted to its initial value ($P_2 = -600$ W to -150 W) at $t = 1.0$ s. Fig. 16(b) illustrates the dynamic performance waveforms for different MMAB topologies during the reference change. In the proposed decoupling structure, the current of port #2 accurately tracks the reference value with minimal impact on the dc terminal voltage of port #3. Conversely, the conventional topology exhibits a voltage undershoot of 1.5 V at port #3

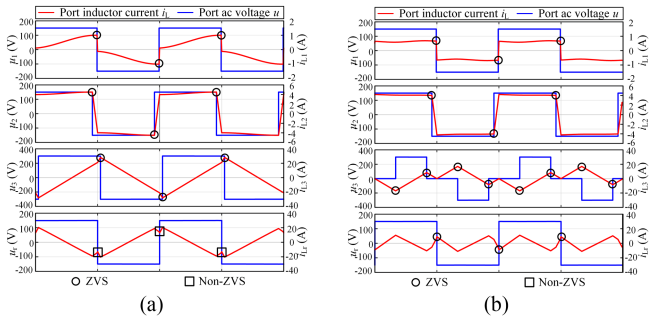

Fig. 17. Simulation results of the port AC terminal voltages and currents of the proposed MMAB converter with relay port. (a) Hard switching without duty ratio control. (b) Soft switching with duty ratio control.

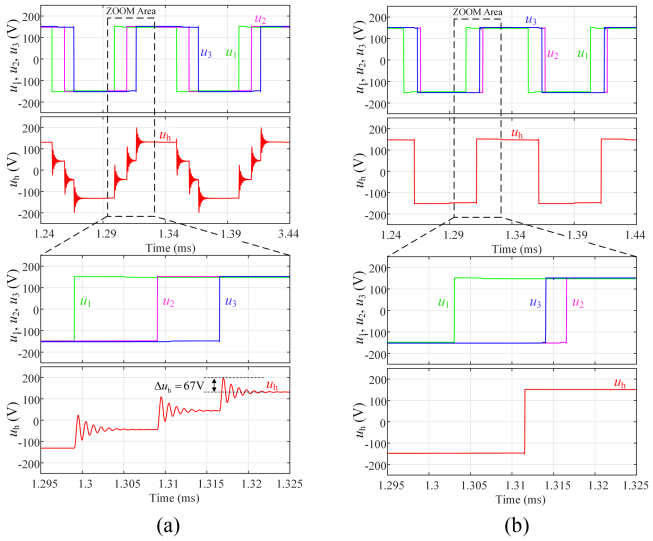

Fig. 18. Simulated HFL voltage waveforms of the MMAB converter. (a) Conventional topology without relay port. (b) Proposed topology with relay port.

when the reference current at port #2 increases, and a voltage overshoot of 1.3 V when the reference current decreases. The decoupling performance of the proposed structure is evident from the dynamic behavior of the port currents and voltage reference changes.

B. ZVS Optimal Method Validation

A simulation is conducted under the condition of an unbalanced voltage conversion ratio and light-load condition to validate the ZVS optimal control. The dc port voltage of port #3 is set to 300 V (dc conversion ratio $M_3 = 2$). The simulation operating points are configured with $P_2 = 600$ W ($i_2 = 4$ A), $P_3 = -620$ W ($R_{\text{load}} = 145\ \Omega$).

Fig. 17 shows simulation waveforms of the port ac terminal voltages and currents of the proposed MMAB converter with relay port. From Fig. 17(a), it can be observed that hard switching occurs at port #r when the duty ratio control is not implemented. Subsequently, duty ratio control is adopted for

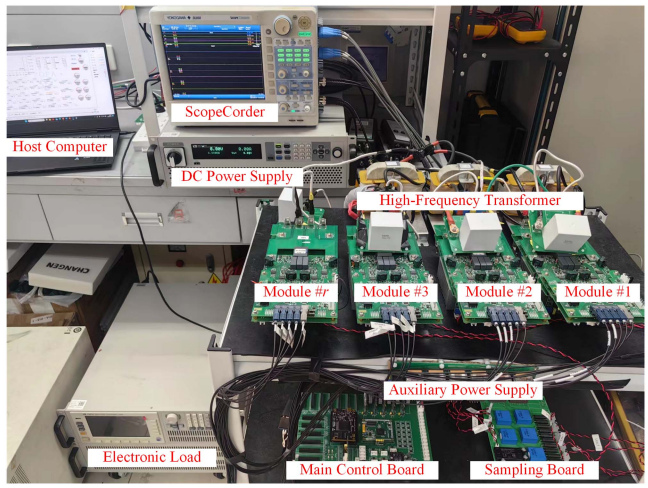

Fig. 19. MMAB experimental prototype.

TABLE III
MAIN PARAMETERS OF THE HFT

Parameter	Value
Magnetizing inductance L_m	900 μH
Core loss equivalent R_m	4 kΩ
Leakage inductance L_s	6 μH
Winding resistance R_s	0.01 Ω
Transformer ratios N	1:1
Self-capacitance of primary winding C_p	100 pF
Self-capacitance of secondary winding C_s	100 pF
Mutual capacitance between two windings C_{ps}	130 pF

port #3, where a duty ratio of $D_3 = 0.5$ is set, as described in Section IV. Fig. 17(b) illustrates the switches in all ports implement ZVS.

Moreover, the implementation of duty ratio control significantly decreases the current stress on port #3 and the relay port #r. Specifically, the peak current at port #3 is reduced from 29 A to 17 A, and the peak current of port #r is reduced from 20 A to 11 A.

C. HFO Suppression Validation

A simulation model of the MMAB converter was developed using LTspice to verify the effectiveness of the proposed topology in suppressing HFO, as shown in Fig. 15. The model of IGBT power devices (IKZ75N65EH5) is obtained from Infineon, Inc. The models of the HFTs are built based on the three-capacitor model, as shown in Fig. 11(b), with specific parameters detailed in Table III. Other system electrical parameters align with those in Table II.

Fig. 18(a) shows the waveforms of the conventional MMAB converter. The peak waveforms of HFL show substantial distortion. The peak voltage of HFL is 199 V, with a voltage oscillation magnitude of approximately 67 V, equating to 50% of the nominal voltage.

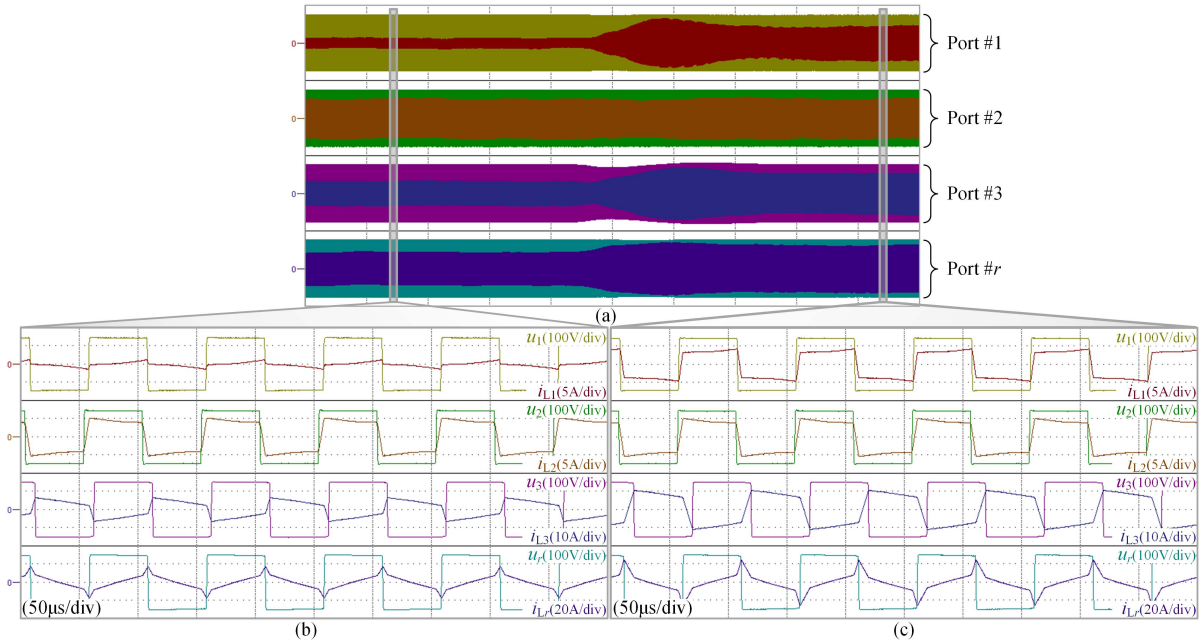

Fig. 20. Experimental waveforms of port AC terminal voltages and currents during sudden power changes. (a) Dynamic operation of the converter during the load on port #3 decreasing from 40 Ω to 20 Ω. (b) Steady-state operation under light-load conditions. (c) Steady-state operation under heavy-load conditions.

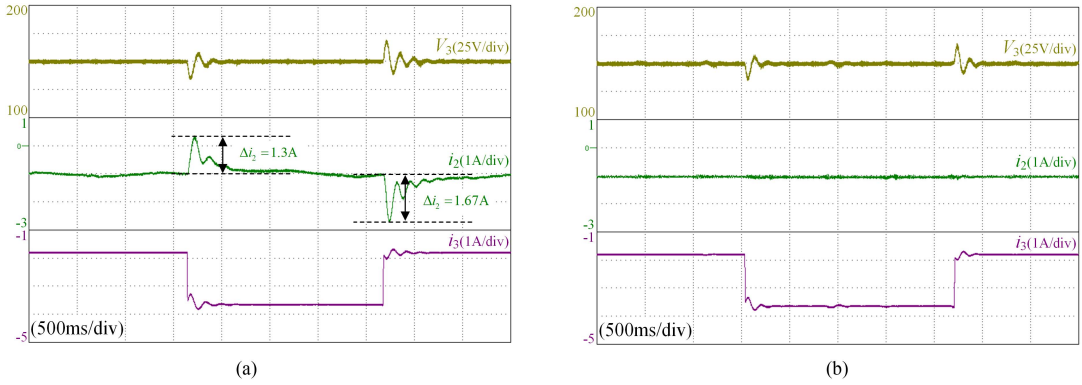

Fig. 21. Transient performance of port voltage and current under a load disturbance at port #3. (a) In the conventional MMAB converter. (b) In the proposed MMAB converter with relay port.

In contrast, Fig. 18(b) illustrates the waveforms of the proposed MMAB topology with the relay port. The voltage waveform of HFL appears as an ideal square wave, which equals the ac terminal voltage of port #*r*. Notably, the oscillation in HFL is clearly suppressed, which verifies the theoretical analysis in Section V.

VII. Experimental Verification

To validate the effectiveness of the proposed decoupling structure of the MMAB converter, ZVS optimal method, and the HFO suppression method, a series of experiments was performed on a four-port MMAB converter prototype, as illustrated in Fig. 19. The schematic of the experimental MMAB prototype aligns with the simulation schematic shown in Fig. 15. The electrical parameters of the prototype are consistent with those of the simulation models, as specified in Tables I and II. The Infineon IKZ75N65EH5 IGBTs were used for the full-bridge modules, with the switching deadtime set at $t_{\mathrm{d}} = 1\ \mu$s. The prototype converter was controlled using a Texas Instruments TMS320F28377D digital signal processor.

A. Typical Operation Waveforms

Fig. 20 illustrates the experimental waveforms of ac terminal voltages and currents during the load on port #3 steps from 40 Ω to 20 Ω. The operating points are set as follows: $P_2 =$ 600 W ($i_2 = 4$ A), $P_3 = -562$ W to -1125 W (R_{load} is varied from 40 Ω to 20 Ω), where the converter operates in two-source one-load (2S-1L) mode. Fig. 20(a) shows the dynamic operation

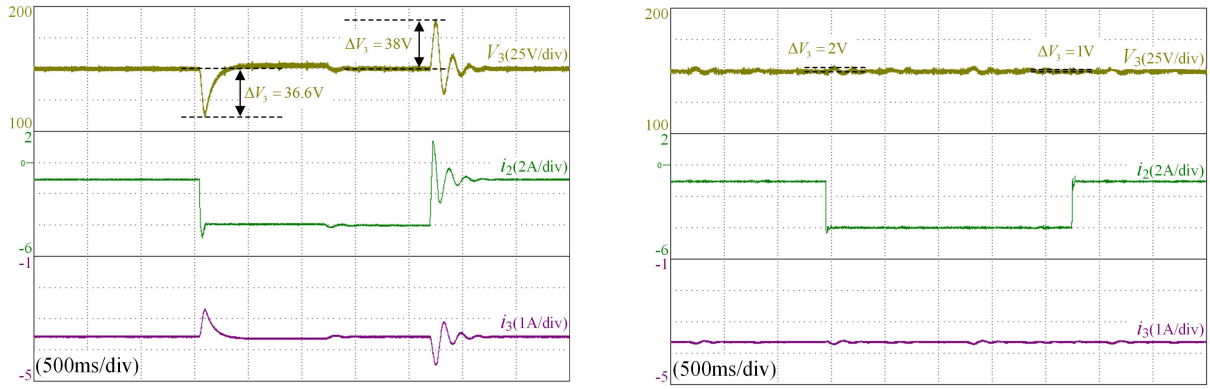

Fig. 22. Transient performance of port voltage and current under a reference current step at port #2. (a) In the conventional MMAB converter. (b) In the proposed MMAB converter with relay port.

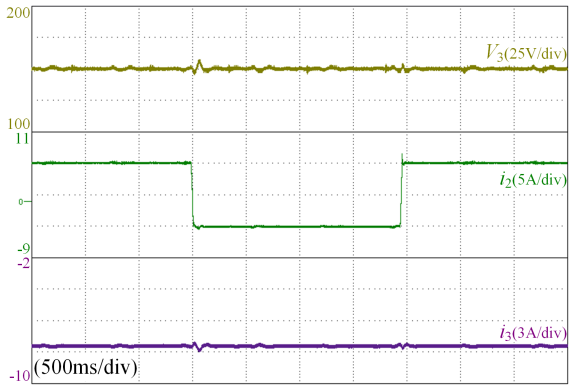

Fig. 23. Bidirectional power transmission performance of port voltage and current under reference current steps at port #2 in the proposed MMAB converter with relay port.

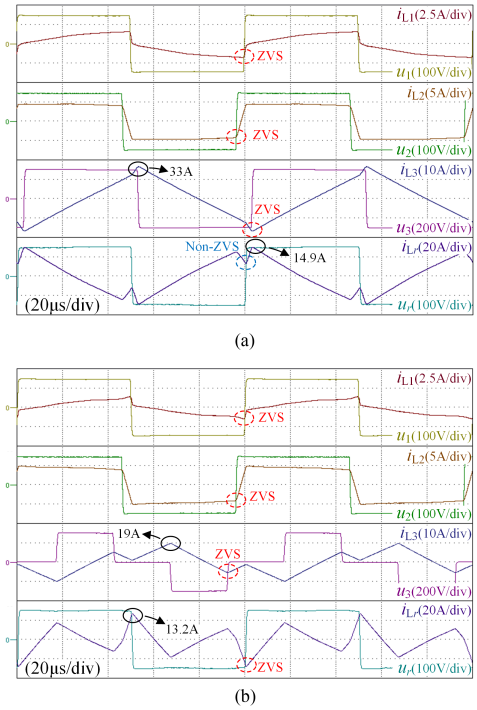

Fig. 24. Experimental results of the port AC terminal voltages and currents of the proposed MMAB converter with relay port. (a) Hard-switching without duty ratio control. (b) Soft-switching with duty ratio control.

of the converter during sudden power changes. Fig. 20(b) and (c) provides detailed insights into the steady-state operation under light-load ($P_3 = -562$ W) and heavy-load ($P_3 = -1125$ W) conditions, respectively. These results validate the MMAB converter with the relay port under the proposed control strategy.

Additionally, Fig. 20 also presents the waveform of the HFL voltage, which is clamped by the port #*r* voltage. Its waveform resembles an ideal square wave, aligning with the simulation results. This indicates that the proposed structure effectively suppresses the HFO in the MMAB converter.

B. Transient Operation Waveforms

To validate the dynamic performance of the proposed MMAB converter structure, two experimental cases were performed on the prototype, consistent with simulation results.

Case Study I: In this case, the converter was tested in one-source and two-load (1S-2L) mode, where a load step was introduced by increasing the load on port #3 by 50% ($P_3 = -281$ W to -562 W) and then returning to the original value ($P_3 = -562$ W to -281 W). This load step was achieved by adjusting the electronic load from 80 Ω to 40 Ω and reverting. Fig. 21 presents a comparison of the results for the conventional and proposed topologies. As shown in Fig. 21(a), the conventional MMAB converter exhibits a current overshoot of 1.3 A in port #2 during the load increase at port #3 and a current undershoot of 1.67 A during the load decrease. In contrast, Fig. 21(b) demonstrates that the proposed topology maintains the port #2 current at -1 A ($P_2 = -150$ W) despite the load disturbance at port #3. This further validates an improved dynamic decoupling performance achieved by the proposed structure.

Case Study II: The experiment also analyzed the effects of varying reference currents. The converter operated in 1S-2L mode. Specifically, the reference current at source port #2 was adjusted from -1 A to -4 A ($P_2 = -150$ W to -600 W) and

subsequently returned to -1 A ($P_2 = -600$ W to -150 W). As shown in Fig. 22(a), when the reference current of port #2 increases to -4 A, the voltage undershoot at port #3 reaches 36.6 V. Similarly, decreasing the reference current leads to a voltage overshoot of 38 V at port #3, which significantly exceeds that of the proposed decoupling structure shown in Fig. 22(b). Consequently, the proposed structure has superior power decoupling performance compared to the conventional topology.

Furthermore, an experiment was conducted with the converter operating at $P_2 = 900$ W ($i_2 = 6$ A), $P_3 = -1125$ W ($R_{\text{load}} = 20\ \Omega$) to validate the bidirectional power transmission performance of the proposed MMAB converter structure. The reference current at the source port #2 was changed from 6 A to -4 A ($P_2 = 900$ W to -600 W) and then reverted to 6 A ($P_2 = -600$ W to 900 W). Fig. 23 confirms the proposed structure's capability for accurate current tracking and efficient bidirectional power transfer without significant voltage impact on port #3.

C. ZVS Operation Waveforms

An experiment was conducted under conditions of an unbalanced voltage conversion ratio and light load to validate the ZVS optimal control method. The operating point was consistent with the simulation detailed in Section VI-B. The converter operated in 2S-1L mode, with $P_1 = 20$ W, $P_2 = 600$ W ($i_2 = 4$ A), $P_3 = -620$ W ($V_3 = 300$ V, $R_{\text{load}} = 145\ \Omega$).

Fig. 24(a) illustrates that hard-switching occurs in port #r without duty ratio control, while Fig. 24(b) shows that all the switches within the converter achieve ZVS when the duty ratio control is adopted. Additionally, implementing duty ratio control reduces the peak current at port #3 from 33 A to 19 A and the rms current from 18 A to 10.2 A. Similarly, for port #r, the peak current reduces from 14.9 A to 13.2 A and the rms current from 8.2 A to 5.7 A.

The efficiency of the MMAB prototype under light load conditions is experimentally measured with a power analyzer (FLUKE NORMA 5000). When operating at 12.4% of the prototype's rated power (5 kW), the efficiency increased from 78.27% (in Fig. 24(a) without duty ratio control) to 83.61% (in Fig. 24(b) with duty ratio control). It is evident that due to its soft-switching operation and the reduced current stress and rms, the efficiency increased significantly by 5.34% under light load conditions.

VIII. Conclusion

In this article, a modified structure of the MMAB converter with a relay port is proposed to achieve hardware-level power decoupling. This configuration introduces an additional port connected to the HFL of the MMAB converter without an HFT and phase-shift inductor. This topology decomposes a coupled MIMO multiport converter into multiple SISO two-port converters without increasing the control complexity. While this approach slightly increases the power components, it demonstrates a significant scalability and sufficient fault tolerance. Furthermore, this structure effectively eliminates the HFO in the MMAB converter. An optimal design and control method is introduced to expand the ZVS operating range. The simulation and experimental results verify the effectiveness of this proposed topology in power flow decoupling, ZVS optimal control and HFO suppression, marking it as a promising MPC topology for versatile power management.

References

[1] S. Falcones, R. Ayyanar, and X. Mao, "A DC–DC multiport-converter-based solid-state transformer integrating distributed generation and storage," *IEEE Trans. Power Electron.*, vol. 28, no. 5, pp. 2192–2203, May 2013.

[2] K. Li et al., "Design and implementation of four-port megawatt-level high-frequency-bus based power electronic transformer," *IEEE Trans. Power Electron.*, vol. 36, no. 6, pp. 6429–6442, Jun. 2021.

[3] J. Lei, H. Ma, G. Qin, Z. Guo, P. Xia, and C. Hao, "A comprehensive review on the power supply system of hydrogen production electrolyzers for future integrated energy systems," *Energies*, vol. 17, no. 4, Feb. 2024, Art. no. 935.

[4] I. Kougioulis, A. Pal, P. Wheeler, and M. R. Ahmed, "An isolated multiport DC–DC converter for integrated electric vehicle on-board charger," *IEEE J. Emerg. Sel. Topics Power Electron.*, vol. 11, no. 4, pp. 4178–4198, Aug. 2023.

[5] G. Buticchi, L. F. Costa, D. Barater, M. Liserre, and E. D. Amarillo, "A quadruple active bridge converter for the storage integration on the more electric aircraft," *IEEE Trans. Power Electron.*, vol. 33, no. 9, pp. 8174–8186, Sep. 2018.

[6] H. Yu, Y. Wang, H. Zhang, and Z. Chen, "Impedance modeling and stability analysis of triple-active-bridge-converter-based renewable-electricity-hydrogen-integrated metro DC traction power system," *IEEE Trans. Ind. Electron.*, vol. 70, no. 12, pp. 12340–12353, Dec. 2023.

[7] F. Ma, X. Wang, L. Deng, Z. Zhu, Q. Xu, and N. Xie, "Multiport railway power conditioner and its management control strategy with renewable energy access," *IEEE J. Emerg. Sel. Topics Power Electron.*, vol. 8, no. 2, pp. 1405–1418, Jun. 2020.

[8] T. Pereira, F. Hoffmann, R. Zhu, and M. Liserre, "A comprehensive assessment of multiwinding transformer-based DC–DC converters," *IEEE Trans. Power Electron.*, vol. 36, no. 9, pp. 10020–10036, Sep. 2021.

[9] P. Zumel, C. Fernandez, A. Lazaro, M. Sanz, and A. Barrado, "Overall analysis of a modular multi active bridge converter," in *Proc. IEEE 15th Workshop Control Model. Power Electron.*, 2014, pp. 1–9.

[10] L. Ortega, P. Zumel, C. Fernández, J. López-López, A. Lázaro, and A. Barrado, "Power distribution algorithm and steady-state operation analysis of a modular multiactive bridge converter," *IEEE J. Emerg. Sel. Topics Power Electron.*, vol. 6, no. 3, pp. 1035–1050, Sep. 2020.

[11] D. Mou et al., "Reactive power minimization for modular multi-active-bridge converter with whole operating," *IEEE Trans. Power Electron.*, vol. 38, no. 7, pp. 8011–8015, Jul. 2023.

[12] P. Koohi, A. J. Watson, J. C. Clare, T. B. Soeiro, and P. W. Wheeler, "A survey on multi-active bridge DC–DC converters: Power flow decoupling techniques, applications, and challenges," *Energies*, vol. 16, 2023, Art. no. 5927.

[13] C. Zhao, S. D. Round, and J. W. Kolar, "An isolated three-port bidirectional DC–DC converter with decoupled power flow management," *IEEE Trans. Power Electron.*, vol. 23, no. 5, pp. 2443–2453, Sep. 2008.

[14] I. Biswas, D. Kastha, and P. Bajpai, "Small signal modeling and decoupled controller design for a triple active bridge multiport DC–DC converter," *IEEE Trans. Power Electron.*, vol. 36, no. 2, pp. 1856–1869, Feb. 2021.

[15] H. Tao, A. Kotsopoulos, J. L. Duarte, and M. A. M. Hendrix, "Transformer-coupled multiport ZVS bidirectional DC–DC converter with wide input range," *IEEE Trans. Power Electron.*, vol. 23, no. 2, pp. 771–781, Mar. 2008.

[16] Y. Chen, P. Wang, H. Li, and M. Chen, "Power flow control in multi-active-bridge converters: Theories and applications," in *Proc. IEEE Appl. Power Electron. Conf. Expo.*, 2019, pp. 1500–1507.

[17] C. Gao et al., "Generalized model of n-Port modular multi-active-Bridge converter with multiple-phase-shift modulation," *IEEE Trans.Transp. Electrific.*, to be published, doi: 10.1109/TTE.2024.3389498.

[18] L. Y. Gao, Y. Dai, D. Mou, K. Chen, and Z. Zhao, "High-frequency current predictive control method for multiactive-bridge converter," *IEEE Trans. Power Electron.*, vol. 37, no. 9, pp. 10144–10148, Sep. 2022.

[19] H. Qin, C. Liu, Y. Shi, M. Liu, and C. Ma, "Prediction-based MIMO control of a multiport magnetic-coupled energy router," *IEEE Trans. Power Electron.*, vol. 39, no. 5, pp. 6409–6420, May 2024.

[20] Y. Cai, C. Gu, J. Li, J. Yang, G. Buticchi, and H. Zhang, "Dynamic performance enhancement of a triple active bridge with power decoupling-based configurable model predictive control," *IEEE Trans. Transp. Electrific.*, vol. 9, no. 2, pp. 3338–3349, Jun. 2023.
[21] S. Bandyopadhyay, Z. Qin, and P. Bauer, "Decoupling control of multiactive bridge converters using linear active disturbance rejection," *IEEE Trans. Ind. Electron.*, vol. 68, no. 11, pp. 10688–10698, Nov. 2021.
[22] S. Gong et al., "Sliding mode control-based decoupling scheme for quadactive bridge DC," *IEEE J. Emerg. Sel. Topics Power Electron.*, vol. 10, no. 1, pp. 1153–1164, Feb. 2022.
[23] J. Han, X. Li, Y. Sun, S. Gong, and S. Huang, "Optimal design and decoupling control of series DC-link voltages for quadruple-active-bridge based UPQC," *Int. J. Electr. Power Energy Syst.*, vol. 140, Sep. 2022, Art. no. 108038.
[24] Y. Cai et al., "A modular modulation decoupling algorithm for multiple active bridge based multiport EV charger," *IEEE J. Emerg. Sel. Topics Power Electron.*, vol. 12, no. 4, pp. 3637–3649, Aug. 2024.
[25] S. Bandyopadhyay, P. Purgat, Z. Qin, and P. Bauer, "A multiactive bridge converter with inherently decoupled power flows," *IEEE Trans. Power Electron.*, vol. 36, no. 2, pp. 2231–2245, Feb. 2021.
[26] Y. Wang, F. Han, L. Yang, R. Xu, and R. Liu, "A three-port bidirectional multi-element resonant converter with decoupled power flow management for hybrid energy storage systems," *IEEE Access*, vol. 6, pp. 61331–61341, 2018.
[27] P. Wang, X. Lu, W. Wang, and D. Xu, "Hardware decoupling and autonomous control of series-resonance-based three-port converters in DC microgrids," *IEEE Trans. Ind. Appl.*, vol. 55, no. 4, pp. 3901–3914, Jul./Aug. 2019.
[28] J. Wu, X. Yan, X. Sun, X. Su, H. Du, and X. Wang, "A series resonant three-port DC–DC converter with decoupling function and magnetic integration," *IEEE Trans. Power Electron.*, vol. 37, no. 12, pp. 14720–14737, Dec. 2022.
[29] X. Zhang, H. Liu, P. Wheeler, and F. Wu, "Research on power decoupling and parameter mismatch of three-port isolated resonant DC–DC converter applied switch-controlled capacitor," *IEEE Trans. Ind. Electron.*, vol. 70, no. 8, pp. 8098–8107, Aug. 2023.
[30] T. Pereira, Y. Wei, Y. Pascal, H. A. Mantooth, and M. Liserre, "Self-tuning multiport resonant DC/DC converter based on actively-controlled inductors for hybrid storage system integration," *IEEE Trans. Power Electron.*, vol. 38, no. 4, pp. 4787–4804, Apr. 2023.
[31] H. Wang, Y. Zeng, S. Ji, Z. Zhao, L. Yuan, and X. Mo, "ZVS soft switching operation region analysis of modular multi active bridge converter under single phase shift control," *IEEE Trans. Ind. Electron.*, vol. 70, no. 7, pp. 6865–6875, Jul. 2023.
[32] H. Wang et al., "Universal phase-shift modulation scheme and efficiency optimization for modular multiactive bridge converter," *IEEE Trans. Ind. Electron.*, vol. 71, no. 7, pp. 7312–7321, Jul. 2024.
[33] R. De Doncker, D. Divan, and M. Kheraluwala, "A three-phase soft-switched high-power-density DC/DC converter for high-power applications," *IEEE Trans. Ind. Appl.*, vol. 27, no. 1, pp. 63–73, Jan./Feb. 1991.
[34] S. Wei, Z. Zhao, L. Yuan, W. Wen, and K. Chen, "Voltage oscillation suppression for the high-frequency bus in modular-multiactive-bridge converter," *IEEE Trans. Power Electron.*, vol. 36, no. 9, pp. 9737–9742, Sep. 2021.
[35] B. Cui, H. Shi, Q. Sun, X. Tang, L. Hong, and B. Zhao, "A novel analysis, design, and optimal methodology of high-frequency oscillation for dual active bridge converters with WBG switching devices and nanocrystalline transformer cores," *IEEE Trans. Power Electron.*, vol. 36, no. 7, pp. 7665–7678, Jul. 2021.
[36] H. Y. Lu, J. G. Zhu, and S. Y. R. Hui, "Experimental determination of stray capacitances in high frequency transformers," *IEEE Trans. Power Electron.*, vol. 18, no. 5, pp. 1105–1112, Sep. 2003.

Changyu Gao (Graduate Student Member, IEEE) was born in Jinan, China, in 1997. He received the B.S. degree in electrical engineering from Shandong University of Science and Technology, Qingdao, China, in 2019. He is currently working toward the Ph.D. degree in electrical engineering with Beijing Jiaotong University, Beijing, China.

His current research interests include multiport dc–dc converters and solid-state-transformers.

Kai Li (Member, IEEE) received the B.S. degree in electrical engineering from Wuhan University, Wuhan, China, in 2011, and the Ph.D. degree in electrical engineering from Tsinghua University, Beijing, China, in 2017.

He was a Visiting Scholar with the Center for Power Electronics Systems, Virginia Tech, Blacksburg, VA, USA, from 2013 to 2015. He was a Postdoctoral Fellow with Tsinghua University, from 2017 to 2019. In 2019, he was with the School of Electrical Engineering, Beijing Jiaotong University, Beijing, China, where he is currently an Associated Professor with the School of Electrical Engineering. His current research interests include solid-state transformer, railway electrification system, modular multilevel converters, and electrolytic hydrogen production converters.

Zhibo Zhang (Graduate Student Member, IEEE) was born in Tieling, China, in 1996. He received the B.S. degree in electrical engineering in 2019 from Beijing Jiaotong University, Beijing, China, where he is currently working toward the Ph.D. degree in power electronics with the School of Electrical Engineering.

His current research interests include railway electrification system and PWM converter.

Fan Yuan (Graduate Student Member, IEEE) was born in Weifang, China, in 1998. He received the B.S. degree in electrical engineering in 2020 from Beijing Jiaotong University, Beijing, China, where he is currently working toward the Ph.D. degree in power electronics.

His current research interests include dc–dc power conversion and high-frequency transformer.

Sheng Zhang was born in Luzhou, China, in 2002. He received the B.S. degree in electrical engineering in 2023 from Beijing Jiaotong University, Beijing, China, where he is currently working toward the M.S. degree in electrical engineering.

His current research interests include dc–dc converters and electrolytic hydrogen production converters.

Xiaojie You (Member, IEEE) was born in Fujian Province, China, in 1964. He received the M.S. degree from the China Agricultural University, Beijing, China, in 1989, and the Ph.D. degree from the Czech Technical University, Prague, Czech Republic, in 2001, both in electrical engineering.

He is currently a Professor and also the Director with Power Electronic Research Institute, School of Electrical Engineering, Beijing Jiaotong University, Beijing, China. His current research interests include ac drive electric locomotive control, switching power control, active power filters, and power quality control.

Chenchen Wang (Senior Member, IEEE) was born in Anhui, China, in 1981. He received the B.S. and Ph.D. degrees in electrical engineering from Tsinghua University, Beijing, China, in 2003 and 2008, respectively.

He is currently a Professor with the School of Electrical Engineering, Beijing Jiaotong University, Beijing, China. His research interests include electric drives and multilevel converters.